



# Modulating crystal growth of formamidinium-caesium perovskites for over 200 cm<sup>2</sup> photovoltaic sub-modules

Tongle Bu<sup>1,2</sup>, Luis K. Ono<sup>1</sup>, Jing Li<sup>2</sup>, Jie Su<sup>3</sup>, Guoqing Tong<sup>1</sup>, Wei Zhang<sup>1</sup>, Yuqiang Liu<sup>1,4</sup>, Jiahao Zhang<sup>1</sup>, Jingjing Chang<sup>3</sup>, Said Kazaoui<sup>5</sup>, Fuzhi Huang<sup>2</sup>, Yi-Bing Cheng<sup>2,6</sup> and Yabing Qi<sup>1</sup>✉

**Upscalable fabrication of efficient and stable perovskite solar modules is urgently needed for commercialization. Here we introduce methylammonium chloride additives in the co-solvent system of *N*-methyl-2-pyrrolidone/*N,N*-dimethylformamide to control the formation of intermediate phases during the growth of formamidinium-caesium lead triiodide perovskite films. We achieve high-quality films upon drying without the use of anti-solvent. By implementing bulk and surface passivation, champion efficiencies of 24.02% for a small-sized solar cell and 20.5% for a 5 cm × 5 cm solar mini-module on an aperture area of 22.4 cm<sup>2</sup> (geometric fill factor ~ 96%) are achieved by spin-coating. The fully blade-coated perovskite solar sub-module demonstrates a champion efficiency of 15.3% on an aperture area of 205 cm<sup>2</sup>. The solar mini-module exhibits impressive operational stability with a  $T_{80}$  lifetime of over 1,000 h at maximum power point tracking under continuous light illumination.**

Due to the outstanding optoelectronic properties of hybrid organic–inorganic metal halide perovskite materials, such as high absorption coefficient, long carrier diffusion length and low trap density, over 25% power conversion efficiencies (PCEs) have been achieved for small-sized perovskite solar cells (PSCs)<sup>1–3</sup>. However, the realization of large-scale, high-efficiency and stable perovskite solar modules (PSMs) still faces a number of technological hurdles for widespread commercial application<sup>4–7</sup>, principally due to a lack of control when upscaling the manufacturing process, which affects perovskite homogeneity and morphology, in turn affecting the reproducibility and long-term stability of PSMs<sup>7,8</sup>.

Recently, an increasing amount of research has been devoted to improving both the PCE and stability of perovskite solar mini-modules from the viewpoints of scalable deposition engineering<sup>4,9</sup>, perovskite composition<sup>10–12</sup>, electron–hole transport material and the corresponding interfaces<sup>13–17</sup>. However, the scalable fabrication of a large-area, high-quality perovskite light-absorbing layer remains elusive. To achieve highly efficient and stable PSMs, typical three-dimensional (3D) formamidinium (FA, NH<sub>2</sub>CH=NH<sub>2</sub><sup>+</sup>)-based lead triiodide perovskite has become a widely studied material due to its narrower bandgap ( $E_g$ ) and better thermal stability compared to its methylammonium (MA, CH<sub>3</sub>NH<sub>3</sub><sup>+</sup>)-based counterparts<sup>18–20</sup>. Various strategies, including hybrid chemical vapour deposition<sup>21</sup>, and one-step and two-step solution processes such as slot-die coating, inkjet printing and spray coating<sup>22–26</sup>, have also been employed to upscale large-area, high-quality FA-based perovskite films. Among these, one-step solution printing techniques such as blade coating and slot-die coating are promising methods that offer low cost and convenience for scalable fabrication<sup>27</sup>, and combined

with suitable additive engineering have demonstrated impressive efficiencies for perovskite solar mini-modules<sup>9,10,23</sup>. For example, Huang and co-workers reported a blade-coated FA-based perovskite solar mini-module with a PCE of over 19% on an aperture area of 50 cm<sup>2</sup> by introducing a solid-state lead-coordinating additive of carbonylhydrazide to modify the interfacial properties between the perovskite and the substrate<sup>28</sup>. Seok and co-workers also reported a bar-coated FA-based perovskite solar mini-module with an efficiency of 20.4% on an aperture area of 31 cm<sup>2</sup> via additive engineering of *n*-cyclohexyl-2-pyrrolidone to improve the morphology of the perovskite layer<sup>29</sup>. However, work on printing perovskite solar sub-modules with an area larger than 200 cm<sup>2</sup> is still lacking. Upscaling high-quality, large-scale perovskite films and assembling them into sub-modules with a minimum PCE penalty still presents a challenge, but is also an essential step towards panel-scale solar cells.

If a compact perovskite film can be formed simply by self-drying (here, self-drying means that the solvent of the perovskite precursor ink volatilizes naturally at room temperature without the assistance of any other process such as heating, spinning, blowing and so on), the upscaling printing process will be easier and more efficient (that is, more convenient, lower cost and higher reproducibility). Based on this rationale, it is essential to develop a suitable perovskite precursor ink for growing high-quality perovskite films for large-scale sub-modules. In our previous study, we described a lead-halide-templated crystallization process for printing large-area FA-based perovskite films that minimized the formation of undesirable perovskite–*N,N*-dimethylformamide (DMF) complex intermediates that could induce dendritic crystals<sup>24,30</sup>. The competition

<sup>1</sup>Energy Materials and Surface Sciences Unit (EMSSU), Okinawa Institute of Science and Technology Graduate University (OIST), Okinawa, Japan.

<sup>2</sup>State Key Laboratory of Advanced Technology for Materials Synthesis and Processing, Wuhan University of Technology, Wuhan, PR China. <sup>3</sup>Xidian University, School of Microelectronics, State Key Discipline Lab of Wide Band Gap Semiconductor Technology, Shaanxi Joint Key Lab of Graphene, Advanced Interdisciplinary Research Center for Flexible Electronics, Xi'an, PR China. <sup>4</sup>College of Textiles & Clothing, State Key Laboratory of Bio-fibers and Eco-textiles, Qingdao University, Qingdao, PR China. <sup>5</sup>Department of Energy and Environment, National Institute of Advanced Industrial Science and Technology (AIST), Tsukuba, Japan. <sup>6</sup>Xianhu Laboratory of the Advanced Energy Science and Technology Guangdong Laboratory, Foshan, PR China.

✉e-mail: [Yabing.Qi@OIST.jp](mailto:Yabing.Qi@OIST.jp)

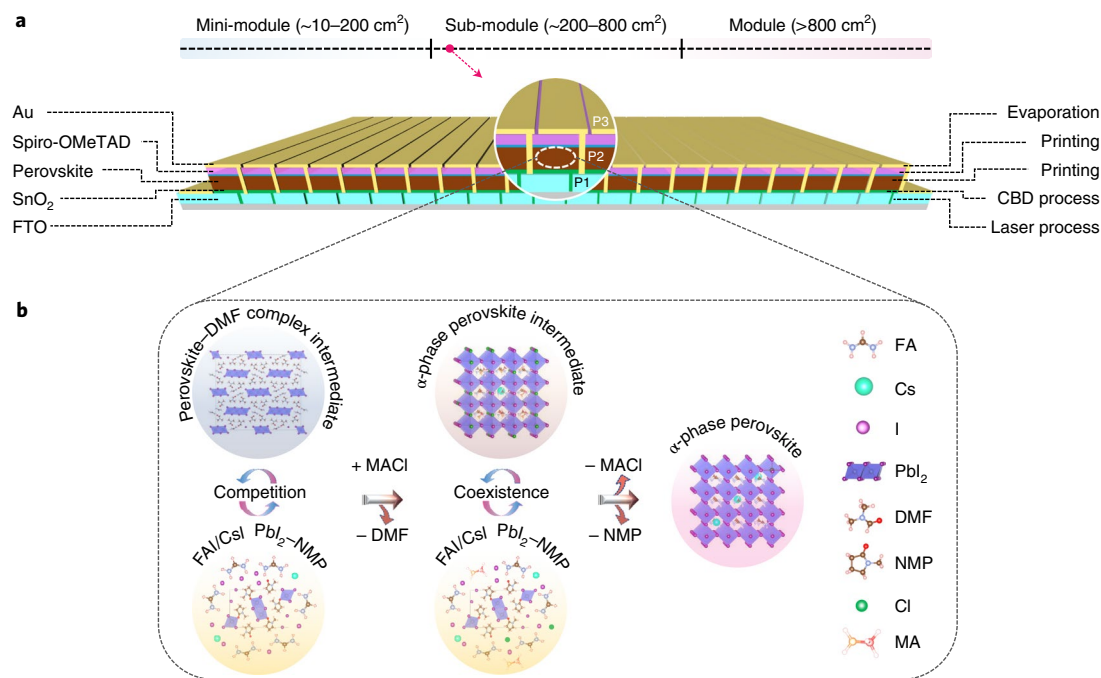


**Fig. 1 | Solar sub-module configuration and intermediate phase-modulated growth strategy for scalable deposition of the perovskite layer.**

**a**, Classifications of perovskite solar modules defined by area<sup>49</sup>, and schematic illustration of the scalable fabrication of the perovskite solar sub-module. The left-hand legend describes each functional layer with the corresponding scalable fabrication methods of each layer on the right. P1–P3, three parting lines in a module. CBD, chemical bath deposition. **b**, Schematic illustration of the phase transition during the insertion and removal of MACl. The initial competition between the perovskite–DMF complex intermediates and the  $\text{PbI}_2$ –NMP adducts is suppressed by the conversion of perovskite–DMF complex intermediates to MACl-incorporated  $\alpha$ -phase perovskite intermediates during crystallization, followed by the final conversion to the  $\alpha$ -phase perovskite with the release of MACl after the ripening process. Adapted with permission from ref. <sup>24</sup>. Copyright 2021, AAAS.

between the lead halide–*N*-methyl-2-pyrrolidone (NMP) adducts and the perovskite–DMF complex intermediates dominates the morphology and crystallinity of the final FA-based perovskite films. The presence of an ample amount of CsI (17%) and lead chloride ( $\text{PbCl}_2$ ) helps to improve the morphology, suppress the  $\delta$ -phase formation and stabilize the final  $\alpha$ -phase perovskite film<sup>31–33</sup>; however, it also enlarges the bandgap and thus lowers the efficiency of the eventual solar modules. The introduction of a suitable amount of MACl additive is another widely used strategy for improving the morphology and stabilizing the  $\alpha$ -phase of FA-based perovskite in the one-step or two-step methods<sup>34–36</sup>. However, the effect of MACl additives on the nucleation and growth of self-drying perovskite films is not fully understood, but knowledge of this effect is essential to overcome the challenges of improving the quality of large-area films.

In this work, we report a modulation strategy for self-drying FA–Cs perovskite precursor ink for the scalable fabrication of large-scale perovskite solar sub-modules. Figure 1a presents the configuration of the perovskite solar sub-module with the scalable deposition strategy of each functional layer. A suitable amount of MACl additives is introduced into a narrower bandgap ( $\sim 1.55$  eV)  $\text{FA}_{0.88}\text{Cs}_{0.12}\text{PbI}_3$  perovskite–NMP/DMF precursor ink to realize the scalable printing of high-quality perovskite layers. In our initial exploration, we found that the lower formation energy of FA–Cs-alloyed perovskites contributed to the growth of high-quality  $\alpha$ -phase films (Supplementary Fig. 1 and Supplementary Note 1). Due to the lower formation energy through the incorporation of MACl in the  $\text{FAPbI}_3$  perovskite crystal structure<sup>34</sup>, we propose that the undesirable FA-based perovskite–DMF complex intermediates, which originally transform into  $\delta$ -phase perovskites, can be directly converted to  $\alpha$ -phase perovskite intermediates with the addition of MACl. From in situ X-ray diffraction studies, we inferred the

corresponding nucleation and growth behaviours with the further introduction of MACl as illustrated in Fig. 1b. In addition, MACl can also induce higher orientation growth of perovskite crystals, resulting in high-quality perovskite films. By further passivating defects around the crystals using excess  $\text{PbI}_2$  and forming 2D perovskite with the long-chain ligands on the 3D perovskite surface, a champion efficiency of 24.02% is achieved on small-sized PSCs. With precise control of the geometric fill factor ( $\sim 96\%$ ) for solar modules, the corresponding  $5\text{ cm} \times 5\text{ cm}$  solar mini-module demonstrates high efficiency of 20.5% on an aperture area of  $22.4\text{ cm}^2$ , corresponding to an active area efficiency of 21.4% and a total area efficiency of 18.4% on a  $25.0\text{ cm}^2$  substrate. More importantly, this strategy can be also translated to even larger scales by scalable printing, enabling a fully blade-coated  $15\text{ cm} \times 15\text{ cm}$  solar sub-module with a high efficiency of 15.3% on an aperture area of  $205\text{ cm}^2$ .

### Self-drying FA–Cs perovskite ink modulation

We first optimized the nucleation and growth processes of the narrower-bandgap perovskite material,  $\text{FA}_{0.88}\text{Cs}_{0.12}\text{PbI}_3$ , to satisfy the scaling-up requirements for a commercial printing process. However, at low concentrations of caesium, intrinsic properties such as formation energy, morphology and especially the crystallization process are notably changed as presented in Supplementary Fig. 1. The introduction of a further 10% molar ratio  $\text{PbCl}_2$  into the perovskite precursor as described in our previous work<sup>24</sup> was still not enough to eliminate the pinholes in the  $\text{FA}_{0.88}\text{Cs}_{0.12}\text{PbI}_3$  perovskite film even after anti-solvent-free spin-coating (Supplementary Fig. 2). To gain further knowledge, the pure  $\text{FA}_{0.88}\text{Cs}_{0.12}\text{PbI}_3$  perovskite film was self-dried on the fluorine-doped tin oxide (FTO) substrate from the NMP/DMF co-solvent system at room temperature. We observed a poor morphology with a lot of rectangular bulk clusters stacking on top of one another (Fig. 2a and Supplementary Fig. 3),

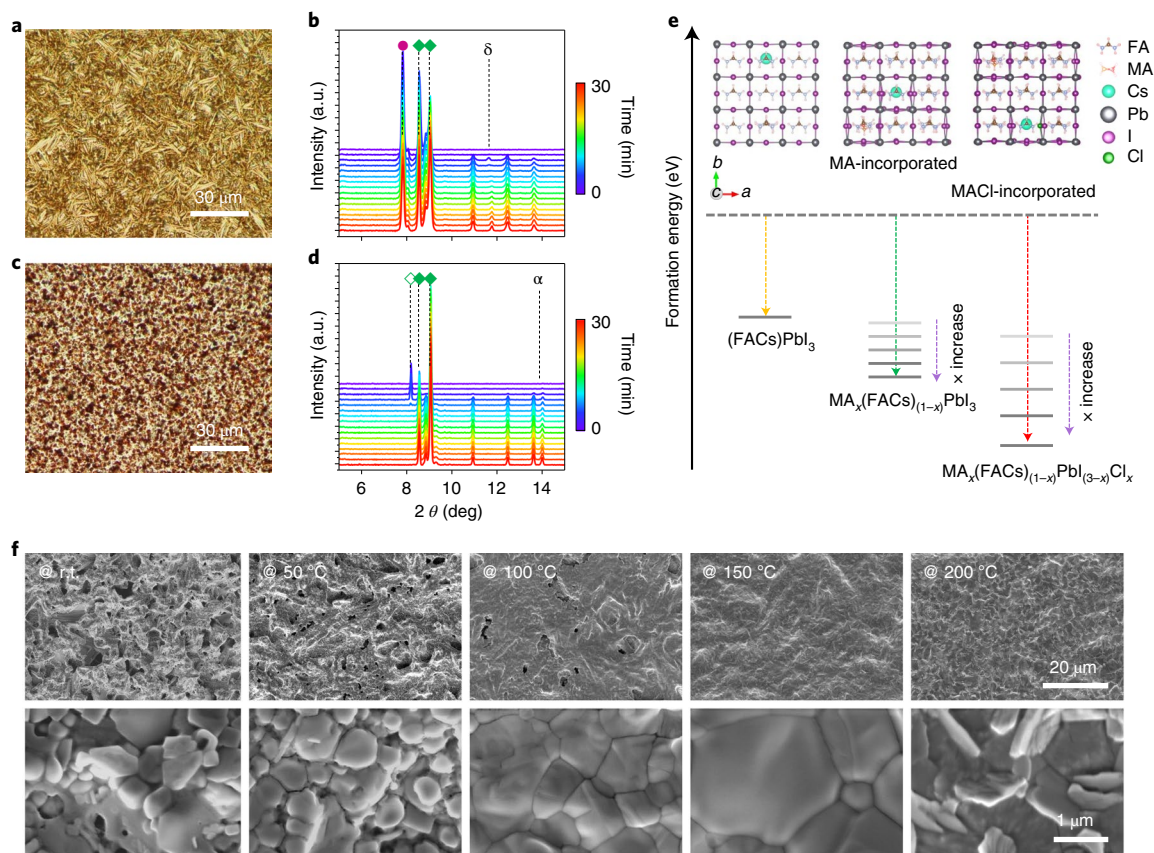


**Fig. 2 | Nucleation and growth process characterization of self-drying perovskite films.** **a–d**, Optical microscopy images (**a,c**) and in situ X-ray diffraction patterns (**b,d**) of the different perovskite inks self-dried on the FTO substrates:  $\text{FA}_{0.88}\text{Cs}_{0.12}\text{PbI}_3\text{-NMP/DMF}$  (**a,b**) and  $\text{FA}_{0.88}\text{Cs}_{0.12}\text{PbI}_3\text{-0.3MACl-NMP/DMF}$  (**c,d**). Purple circle,  $\text{FA}_2\text{Pb}_3\text{I}_8\text{-4DMF}$ ; solid green diamond,  $\text{PbI}_2\text{-NMP}$ ; open diamond,  $\text{PbX}_2\text{-0.5NMP-0.5DMF}$  (ref. <sup>24</sup>). **e**, Schematic diagram of the formation energy changes of the  $(\text{FA}_{26/27}\text{Cs}_{1/27})\text{PbI}_3$  perovskite with the incorporation of MA and MACl, respectively ( $x \leq 1/3$ ). The horizontal grey dashed line represents the baseline of energy (that is, the formation energy of pure  $\text{FAPbI}_3$ ), and the top sketches show the corresponding perovskite crystal structures viewed along the *c* axis. **f**, SEM images of the self-dried films from  $\text{FA}_{0.88}\text{Cs}_{0.12}\text{PbI}_3\text{-0.3MACl-NMP/DMF}$  precursor ink and of films annealed at different temperatures for 10 min.

which was induced by the formation of stronger  $\text{FA}_2\text{Pb}_3\text{I}_8\text{-4DMF}$  intermediates than the  $\text{PbI}_2\text{-NMP}$  adducts as demonstrated by the in situ X-ray diffraction results (Fig. 2b). Therefore, the strong competitiveness of the DMF-coordinated perovskite complex intermediates during the nucleation process contributes to the poor morphology of the final perovskite films.

To further suppress the perovskite–DMF complex intermediates, instead of introducing excessive  $\text{PbCl}_2$  (Supplementary Fig. 2), we find that these intermediates can be completely suppressed by the introduction of MACl, most of which leaves the perovskite film eventually and does not substantially enlarge the optical bandgap of the perovskite<sup>34</sup>. By introducing MACl at a molar ratio of 0.3 to the stoichiometric perovskite precursor, more nuclei form with smaller cluster sizes as shown in Fig. 2c. The  $\text{FA}_2\text{Pb}_3\text{I}_8\text{-4DMF}$  intermediates that originally transform to  $\delta$ -phase are completely suppressed according to the in situ X-ray diffraction study (Fig. 2d). More interestingly, the  $\alpha$ -phase perovskite directly forms and becomes predominant at the expense of the  $\delta$ -phase during solvent evaporation. Even without the assistance of NMP, which helps lower the free energy<sup>24,37</sup>, the  $\alpha$ -phase perovskite also forms in the pure DMF system with the addition of MACl additives (Supplementary Fig. 4). This rapid formation of  $\alpha$ -phase perovskite can be ascribed to the lower formation energy due to the incorporation of MACl as demonstrated by the theoretical calculation results (Fig. 2e and Supplementary Fig. 5), which confirm that MACl is incorporated

into the  $\text{FAPbI}_3$  perovskite crystal structure in preference to CsI during the initial crystallization process, thereby stabilizing the formation of  $\alpha$ -phase (black phase). Therefore, the undesirable growth of  $\text{FA}_2\text{Pb}_3\text{I}_8\text{-4DMF}$  intermediates from the pristine precursor ink can be directly converted into  $\alpha$ -phase perovskite intermediates with the addition of MACl, as depicted in the schematic in Fig. 1b, which improves the competitiveness of  $\text{PbI}_2\text{-NMP}$  adducts and suppresses the undesirable  $\delta$ -phase formation, contributing to a denser morphology. As a result, a much denser film can be obtained after self-drying at room temperature as shown in the scanning electron microscopy (SEM) images (Fig. 2f).

### Self-driven compact FA–Cs perovskite during ripening

Thermal annealing at different temperatures is employed to observe the crystal growth and corresponding morphology changes. Figure 2f shows the SEM images of the self-dried films with MACl additives after thermal annealing at different temperatures. As the temperature increases, smaller grains fuse into one larger grain and the holes disappear, while simultaneously the solvent and MACl (or their by-products) are volatilized, as confirmed by the mass spectroscopy analysis (Supplementary Fig. 6), which suggests that the overall mechanism is consistent with a typical Ostwald ripening process, as depicted in Fig. 3a. A pinhole-free compact perovskite film with micro-sized grains and high crystallinity is readily obtained after thermal annealing at 150 °C; however, a further increase in

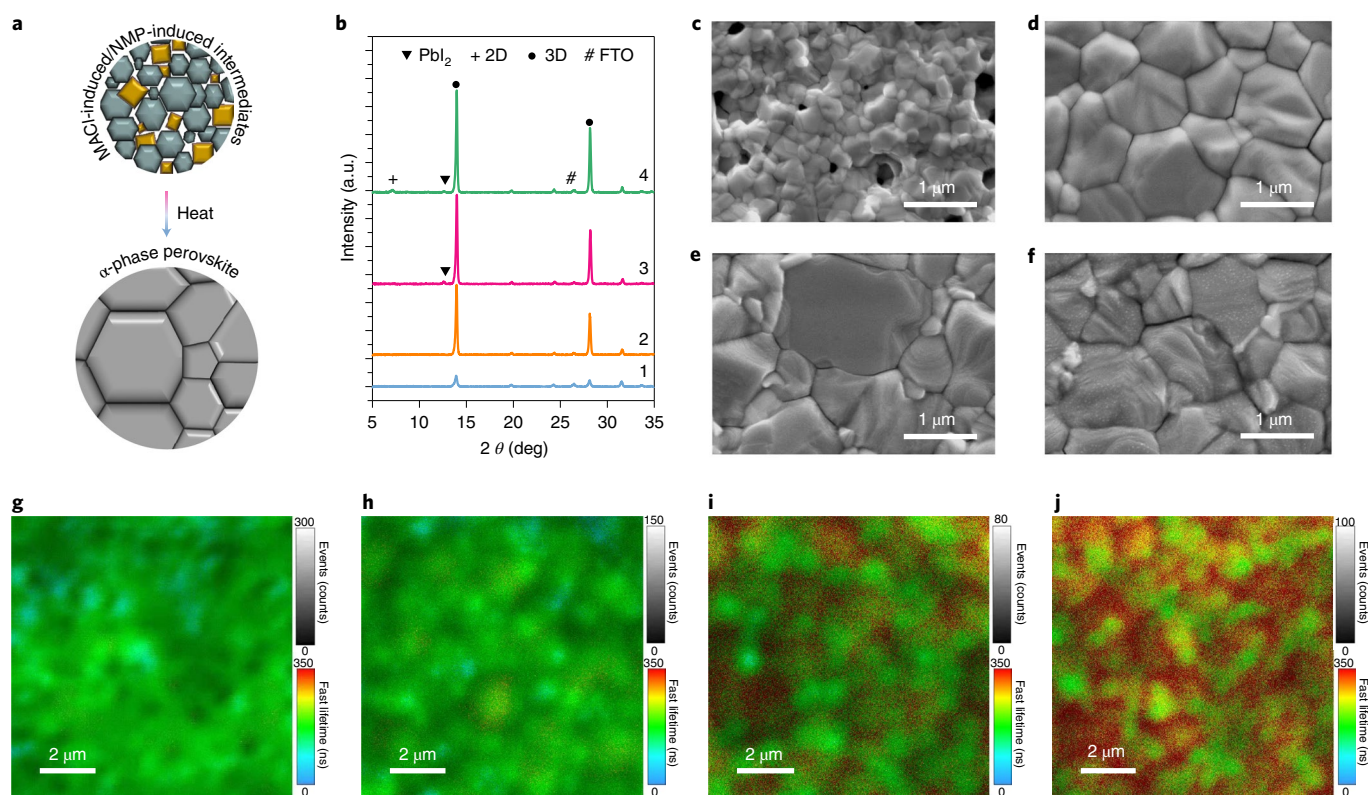


**Fig. 3 | Morphology and defect modulation.** **a**, Schematic diagram of the Ostwald ripening, which involves a phase transition of the MACl-induced perovskite intermediate (grey shape) and NMP-induced  $\text{PbI}_2$ -NMP solvate intermediate (yellow shape) to the final  $\alpha$ -phase perovskite. **b**, X-ray diffraction patterns of spin-coated perovskite films with different additives after thermal annealing: (1)  $\text{FA}_{0.88}\text{Cs}_{0.12}\text{PbI}_3$ -NMP/DMF, (2)  $\text{FA}_{0.88}\text{Cs}_{0.12}\text{PbI}_3$ -0.3MACl-NMP/DMF, (3)  $\text{FA}_{0.88}\text{Cs}_{0.12}\text{PbI}_3$ -0.05 $\text{PbI}_2$ -0.3MACl-NMP/DMF and (4)  $\text{FA}_{0.88}\text{Cs}_{0.12}\text{PbI}_3$ -0.05 $\text{PbI}_2$ -0.3MACl-NMP/DMF with DABr post-treatment. **c–f**, SEM images (**c–f**) and time-resolved confocal photoluminescence mappings (**g–j**) of perovskite films 1–4 in **b**, respectively, after thermal annealing. Note that the average carrier lifetime data (colour scale bars) and the event count data (grey scale bars) have been merged together in **g–j**.

temperature leads to the rapid decomposition of perovskite into  $\text{PbI}_2$  due to the volatilization of FA (Supplementary Fig. 7a,b). In sharp contrast, without MACl additives, the perovskite film shows small size grains and conspicuous pinholes (Supplementary Fig. 3b). This indicates that the introduction of MACl can induce the formation of a compact film easily from the self-drying precursor ink after ripening.

To reduce the surface roughness caused by non-uniform solvent evaporation under self-drying, we find that a simple spin-coating process is suitable to deposit a smoother and denser film with much smaller nuclei. Furthermore, a highly orientated perovskite film with compact morphology and a smooth surface is easily achieved by this MACl-induced Ostwald ripening process, while the pristine counterpart (without MACl) from the anti-solvent-free spin-coating still presents poor crystallinity and obvious pinholes even after thermal annealing (Fig. 3b,c and Supplementary Fig. 11). To further understand the crystal growth behaviour during the Ostwald ripening process with MACl additives, X-ray diffraction characterization was conducted for the spin-coated films after thermal annealing at different temperatures as shown in Supplementary Fig. 7. A new diffraction peak appeared at  $9.3^\circ$  under low-temperature annealing, which is possibly a mixed MACl- and Cs-based new phase perovskite as demonstrated (Supplementary Fig. 8). This peak disappeared when the temperature was over  $75^\circ\text{C}$  due to the volatilization of MACl as confirmed by the mass spectroscopy results (Supplementary Fig. 6), leading to a blended structure of Cs- and FA-based perovskite after the removal of MACl, and subsequently generating FA–Cs–mixed cation-based perovskite films. Therefore, the crystallization process can be described by the two

paths as shown in Supplementary Fig. 9. One path forms the stable  $\text{PbI}_2$ -NMP adducts, and the other path, which originally forms the perovskite–DMF complex intermediates, is directly converted into  $\alpha$ -phase (MAFACs) $\text{Pb}(\text{I})_3$  perovskite intermediates with the insertion of MACl. With the further volatilization of NMP during the ripening process, some of the released  $\text{PbI}_2$  can react with the residual formamidinium iodide (FAI), CsI and MACl to form this new intermediate phase and  $\alpha$ -phase (MAFACs) $\text{Pb}(\text{I})_3$  perovskite intermediates at low temperature. Finally, the mixed-cation-based perovskite ( $\text{FA}_{0.88}\text{Cs}_{0.12}\text{PbI}_3$ ) structure forms due to the release of MACl under higher-temperature ripening, which suppresses  $\delta$ -phase formation during the entire growth process.

More importantly, this MACl-induced cation and anion exchange during the crystallization process not only improves the morphology but also stabilizes the  $\alpha$ -phase FA–Cs perovskite films. Even without thermal annealing, the nuclei formed in the MACl-added films continue to grow into larger, micron-sized polygonal grains (Supplementary Fig. 10). The results also demonstrated the formation of a stable  $\alpha$ -phase and no  $\delta$ -phase even after 60 min in the ambient environment (temperature,  $\sim 25^\circ\text{C}$ ; relative humidity,  $\sim 50\%$ ), while the films without MACl remain small crystals and are converted to  $\delta$ -phase directly (Supplementary Fig. 10). Therefore, this growth strategy is potentially suitable for the scalable fabrication of large-size perovskite films in an ambient environment.

### Defect modulation

To further improve the quality of the perovskite films, we employ a simple passivation strategy for the grain boundaries that involves introducing a suitable excess of  $\text{PbI}_2$  (5% molar ratio) into the

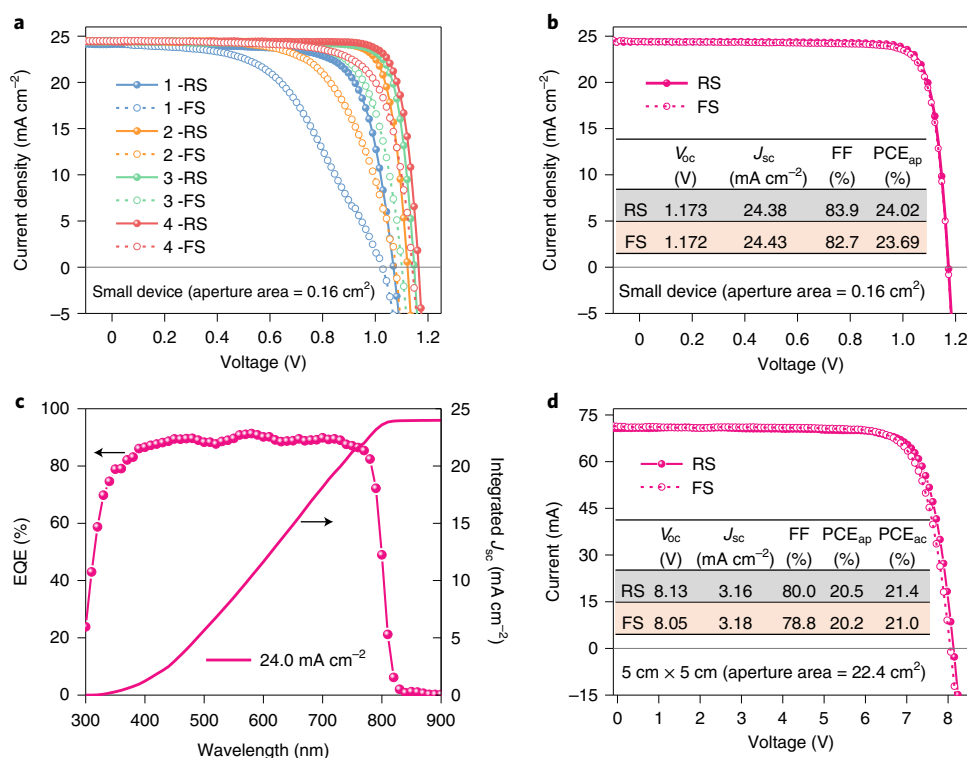


**Fig. 4 | Photovoltaic performance characterization.** **a**, Typical  $J$ - $V$  curves of devices based on different perovskite films: (1)  $\text{FA}_{0.88}\text{Cs}_{0.12}\text{PbI}_3$ -NMP/DMF, (2)  $\text{FA}_{0.88}\text{Cs}_{0.12}\text{PbI}_3$ -0.3MAcI-NMP/DMF, (3)  $\text{FA}_{0.88}\text{Cs}_{0.12}\text{PbI}_3$ -0.05 $\text{PbI}_2$ -0.3MAcI-NMP/DMF and (4)  $\text{FA}_{0.88}\text{Cs}_{0.12}\text{PbI}_3$ -0.05 $\text{PbI}_2$ -0.3MAcI-NMP/DMF with DABr post-treatment. FS, forward scan; RS, reverse scan. **b,c**,  $J$ - $V$  curves (**b**) and EQE spectrum (**c**) of the champion device with  $\text{KPF}_6$  additive. **d**,  $J$ - $V$  curves of the champion 5 cm  $\times$  5 cm perovskite solar mini-module with a series connection of seven subcells. PCE<sub>ap</sub>, aperture area efficiency; PCE<sub>ac</sub>, active area efficiency;  $V_{oc}$ , open-circuit voltage;  $J_{sc}$ , short-circuit current density; FF, fill factor.

precursor ink as per previous reports<sup>38</sup>, and post-treatment with organic salts (dodecylamine hydrobromide, DABr) to passivate both the boundaries and the surface of the grains, respectively. The corresponding crystallinity and morphology changes are shown in Fig. 3b–f and Supplementary Fig. 11. The solubility of MAcI in the stoichiometric perovskite ( $\text{FA}_{0.88}\text{Cs}_{0.12}\text{PbI}_3$ ) precursor solution can also be improved by the reaction with the introduced excess  $\text{PbI}_2$ , which avoids the formation of flocculent precipitates with caesium precursors (Supplementary Fig. 12). The post-treatment with DABr will form a 2D layer perovskite by the reaction with the introduced excess  $\text{PbI}_2$  or cation exchange due to the isopropanol (IPA) solvent, which can slightly dissolve some of the FA molecules and thus enlarge the bandgap of the perovskite films (Supplementary Figs. 13 and 14). The resulting 2D layer serves as a superhydrophobic protective layer with a large water contact angle of over 90° due to the long carbon chain (Supplementary Fig. 13j), and thus greatly improves the stability of the corresponding devices.

To visualize the defect passivation effect achieved with the above strategies, time-resolved confocal photoluminescence microscopy was performed to characterize the charge carrier lifetime of these perovskite films in microdomains (10  $\mu\text{m}$   $\times$  10  $\mu\text{m}$ ) as shown in Fig. 3g–j. There was no obvious difference in the lifetime of perovskite films with or without MAcI additives, both of which show a uniform green region. However, it can be seen that the brighter grains and darker boundaries are clear for the film with MAcI additives. After the introduction of excess  $\text{PbI}_2$ , the dark boundaries transition to a light red with a longer photoluminescence lifetime, indicating that the excess  $\text{PbI}_2$  passivates the grain boundaries effectively. Moreover, the post-treatment of the perovskite film with DABr turns a relatively large fraction of the film into a red and yellow region, which means that the photoluminescence lifetime

is greatly enhanced. These results indicate that this series of processes can effectively passivate the perovskite grains and/or surface to reduce the trap-induced or non-radiative recombination in the films, which would be beneficial to improve the performance of the corresponding devices.

### Anti-solvent-free spin-coated solar cells

To evaluate the photovoltaic performance of these perovskite films through the above strategies, a standard structure of FTO/SnO<sub>2</sub>/perovskite/spiro-OMeTAD/Au (spiro-OMeTAD = 2,2',7,7'-tetrakis[*N,N*-bis(*p*-methoxyphenyl)amino]-9,9'-spirobifluorene) is employed as shown in the energy-level diagram (Supplementary Fig. 15), which exhibits a more preferable energy-level alignment for charge transport with bulk and surface passivation. The champion  $J$ - $V$  curves of the corresponding devices based on these different spin-coated perovskite films without the use of anti-solvent are shown in Fig. 4a. The pristine device with the  $\text{FA}_{0.88}\text{Cs}_{0.12}\text{PbI}_3$  perovskite as the light absorber layer exhibits a relatively low efficiency of 18.99% with large hysteresis. With the modulation induced by MAcI, a notable improved efficiency of over 22% is achieved. The efficiency can be further improved to over 23% by the introduction of excess  $\text{PbI}_2$ . Finally, after post-treatment with DABr, a much higher efficiency of close to 24% was achieved, mainly because the open-circuit voltage ( $V_{oc}$ ) was dramatically improved by passivating the defects and subsequently reducing the charge recombination. All the detailed parameters derived from the  $J$ - $V$  curves are summarized in Supplementary Table 1. The corresponding statistical distribution of photovoltaic parameters for these different perovskite-based devices shows a clear improvement tendency by this series of processing strategies (Supplementary Fig. 16). The typical steady-state output efficiencies for the different devices are

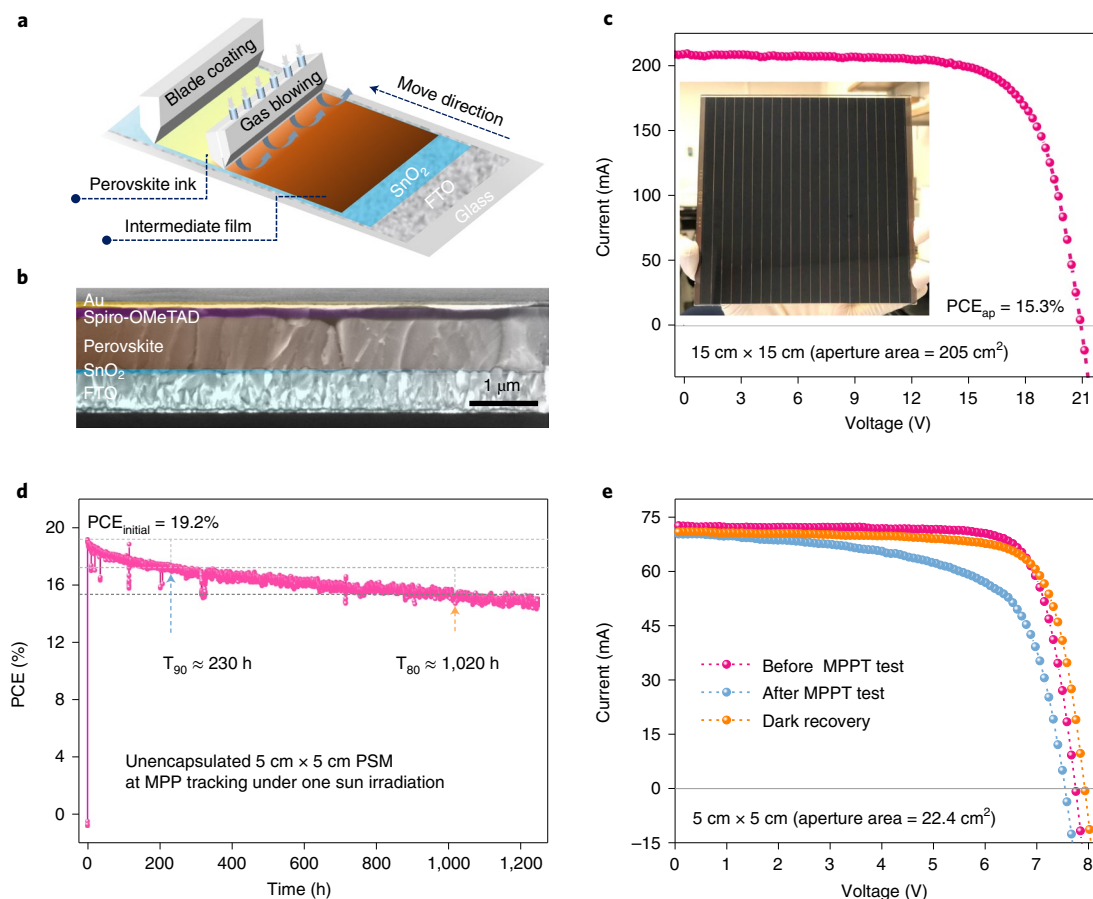


**Fig. 5 | Scalable printing and stability characterization.** **a**, Schematic illustration for the scalable blade coating of large-area perovskite films. **b**, Cross-section SEM image of the fully blade-coated perovskite solar sub-module. **c**,  $I$ - $V$  curve of the champion 15 cm × 15 cm perovskite solar sub-module. Inset: photograph of the corresponding sub-module with a series connection of 21 subcells. **d,e**, Operational stability test of a 5 cm × 5 cm perovskite solar mini-module (aperture area, 22.4 cm<sup>2</sup>) under MPPT (unencapsulated device, in nitrogen atmosphere, at -30 °C) (**d**) and the corresponding  $I$ - $V$  curves before and after MPPT test and after dark storage (**e**).

shown in Supplementary Fig. 17. However, the devices still show an obvious hysteresis.

To further suppress the hysteresis, we introduced KPFA<sub>6</sub> additives into the precursor ink according to our previous report<sup>24</sup>. A champion efficiency of 24.02% is obtained for the optimized device with negligible hysteresis (Fig. 4b). The corresponding integrated  $J_{sc}$  of 24.0 mA cm<sup>-2</sup> obtained from the external quantum efficiency (EQE) spectra matches well with the measured  $J_{sc}$  from the  $J$ - $V$  characterization (Fig. 4c). Typical devices also exhibit good light soaking stability and thermal stability, which delivered an expectant  $T_{80}$  (the time over which the device efficiency drops to 80% of its initial value) lifetime of over 1,000 h at maximum power point (MPP) under one-sun irradiation and an average ~90% efficiency retention after 20 d at 65 °C (Supplementary Fig. 18). We also demonstrate high-efficiency perovskite solar mini-modules on 5 cm × 5 cm substrates with a high geometric fill factor (~96%) by precise control of the P1-P2-P3 process (Supplementary Fig. 19). The corresponding 5 cm × 5 cm solar mini-module demonstrates a high efficiency of 20.5% on an aperture area of 22.4 cm<sup>2</sup>, which corresponds to an active area efficiency of 21.4% and a total area efficiency of 18.4% on a 25.0 cm<sup>2</sup> substrate, respectively (Fig. 4d).

### Scalable printed solar sub-modules

Scalability and stability are currently the two major obstacles to realizing the commercial application of perovskite solar cells. By the modulation of self-drying FA-Cs perovskite ink through this series

of strategies, a large-area high-quality and stable perovskite film can be blade coated in a simple glovebox with rough control of the local atmosphere (temperature, 15 ± 5 °C; relative humidity, 15 ± 5%, where a lower temperature is helpful to initiate the crystallization process after formation of uniform nuclei<sup>39</sup> and lower humidity is helpful to facilitate the nucleation process, thus contributing to a denser and smoother morphology as shown in Supplementary Fig. 20 and Supplementary Note 2). Figure 5a illustrates the printing of large-size perovskite films by a blade-coating set-up with an additional gas-assisted drying system, which enables fast and homogeneous volatilization of the host solvent and results in a uniform and dark black large-area perovskite film. Characterization results performed on five different locations on the large-area 15 cm × 15 cm perovskite film indicate that the scalable printed film possesses a high level of uniformity (Supplementary Fig. 21). By contrast, without the modulation of the precursor ink, the large-area film has a porous nature, and as a result the perovskite solar cell performance is substantially lower (Supplementary Fig. 22).

We then used the blade-coated, high-quality, large-area perovskite films to fabricate 15 cm × 15 cm perovskite solar sub-modules, which is only limited by the processing scale of our laser machine and evaporation system. A uniform purple spiro-OMeTAD film is achieved on the top of this uniform perovskite substrate by blade coating (Supplementary Fig. 23a,b). The cross-sectional SEM image of the perovskite solar module shows a uniform perovskite layer with micro-size grains sandwiched by a

uniform spiro-OMeTAD layer and a thin SnO<sub>2</sub> layer (Fig. 5b and Supplementary Fig. 23c). Photographs and the design of the P1–P2–P3 pattern of a 15 cm × 15 cm perovskite solar sub-module are shown in Supplementary Fig. 24. With these strategies we obtained a champion efficiency of 15.3% for a 15 cm × 15 cm perovskite solar sub-module containing 21 subcells with an aperture area of 205 cm<sup>2</sup> as shown in Fig. 5c. Supplementary Fig. 25a,b shows a typical reverse and forward scan of a large 15 cm × 15 cm perovskite solar sub-module, and the MPP output current density. Supplementary Fig. 25c shows the efficiency distribution of 15 cm × 15 cm perovskite solar sub-modules that were fabricated on different days. The module efficiencies from different upscaling methods with different aperture areas over 150 cm<sup>2</sup> are summarized in Supplementary Fig. 25d and Supplementary Table 2. The photovoltaic conversion efficiency of the high-quality perovskite films obtained in this work using intermediate phase-modulated strategies is higher than previously reported for comparable sizes and printing technologies, indicating the great promise of our approach for scalable printing of large-size perovskite solar panels. To further understand the PCE difference between the small area cells and sub-modules and their origins, we measured the *J*–*V* curves of the small cells (Supplementary Fig. 25e,f and Supplementary Table 4), which were cut at five different locations from a 15 cm × 15 cm sub-module. The relatively small difference in PCE between the separately prepared small cells (PCE, ~24%) and the small cells cut from the 15 cm × 15 cm sub-module (PCE, ~21%) indicates that the relatively large PCE difference between the separately prepared small cells (PCE, ~24%) and the 15 cm × 15 cm sub-modules (PCE, ~15%) is due not only to film uniformity issues when upscaling solar cells from small areas to large areas and fabrication environmental condition differences between small-cell fabrication and large-area sub-module fabrication, but also to other factors (sheet resistance of FTO substrates, issues related to laser scribing, and so on).

In addition, we also characterized the operational stability of the solar mini-module as shown in Fig. 5d and Supplementary Fig. 26, which exhibited a *T*<sub>80</sub> lifetime over 1,000 h at maximum power point tracking (MPPT) under one-sun irradiation. The initial output PCE of 19.2% is consistent with the efficiency (19.5%) derived from the *J*–*V* curve (Fig. 5e and Supplementary Table 3). Interestingly, although the efficiency of the mini-module dropped to 15.3% after exposure to light for over 1,000 h, it almost reversibly recovered to 19.1% after storage in the dark. Therefore, this modulation strategy of the FA–Cs perovskite precursor ink provides a promising technology for scalable manufacturing of efficient and relatively stable large-scale perovskite solar modules.

## Conclusion

We report an efficient upscaling fabrication strategy for high-quality and stable FA–Cs perovskite films by modulating crystal growth from the self-drying precursor ink without the use of anti-solvent. The obstacles to the formation of high-quality FA<sub>0.88</sub>Cs<sub>0.12</sub>PbI<sub>3</sub> perovskite films have been overcome via this strategy through the addition of MAcl in the co-solvent system of DMF/NMP, which dramatically lowers the formation energy and enlarges the crystal size of the perovskite films, contributing to the successful scalable deposition of large-area, high-quality stable perovskite films. For small-sized solar cells, a high efficiency of 24.02% is achieved by further passivation of both the grain boundaries and surface via an in situ formed excess of PbI<sub>2</sub> and the corresponding formed 2D capping layer, and by KPF<sub>6</sub> additives. For solar mini-modules, a relatively high efficiency of 20.5% on an aperture area of 22.4 cm<sup>2</sup> with a high geometric fill factor of 96% is demonstrated for a 5 cm × 5 cm solar mini-module. For large-scale solar sub-modules fabricated by a blade-coating technique, a champion efficiency of 15.3% with an aperture area of 205 cm<sup>2</sup> is demonstrated. In

addition, the solar mini-modules exhibit impressive stability with a *T*<sub>80</sub> lifetime of over 1,000 h at MPPT under one-sun illumination. We expect that our modulation strategy of the precursor ink will pave the way towards the commercial production of high-performance and stable perovskite solar modules in the near future.

## Methods

**Materials.** All reagents were used as received without any further purification, including CsI (99.999% trace metals basis, Sigma-Aldrich), PbI<sub>2</sub> (99.99%, TCI), FAI (Xi'an Polymer Light Technology), MAcl (Xi'an Polymer Light Technology), spiro-OMeTAD (99.8%, Xi'an Polymer Light Technology), 4-*tert*-butylpyridine (99.9%, Sigma-Aldrich), bis(trifluoromethane)sulfonimide lithium salt (Li-TFSI, Sigma-Aldrich), FK209 Co(III) TFSI salt (Sigma-Aldrich), acetonitrile (99.9%, Sigma-Aldrich), chlorobenzene (99.8%, Wako), potassium hexafluorophosphate (KPF<sub>6</sub>, Sigma-Aldrich), SnCl<sub>2</sub>·2H<sub>2</sub>O (99.99%, Sigma-Aldrich), urea (Sigma-Aldrich), thioglycolic acid (Sigma-Aldrich), HCl (Wako), DMF (Wako), NMP (Sigma-Aldrich), DABr (TCI), IPA (Wako).

**Precursor solution preparation.** The different perovskite precursor solutions were prepared based on a stoichiometric composition of FA<sub>0.88</sub>Cs<sub>0.12</sub>PbI<sub>3</sub>–NMP perovskite materials dissolved in DMF solvent with further addition of different amounts of MAcl, PbI<sub>2</sub> and KPF<sub>6</sub> (with molar ratios to perovskite as mentioned in the main text). If we take the FA<sub>0.88</sub>Cs<sub>0.12</sub>PbI<sub>3</sub>–0.3MAcl–NMP/DMF solution as an example, 151.4 mg FAI, 31.2 mg CsI, 461 mg PbI<sub>2</sub>, 20.3 mg MAcl and 96 μl NMP are dissolved in 500 μl DMF to form the precursor solution. The spiro-OMeTAD solution was prepared by dissolving 90 mg spiro-OMeTAD in 1 ml chlorobenzene, adding 21 μl Li-TFSI (from 520 mg ml<sup>-1</sup> stock acetonitrile solution) and 11 μl FK209 (300 mg ml<sup>-1</sup> stock acetonitrile solution) and 35 μl 4-*tert*-butylpyridine.

**Small-size perovskite solar cell fabrication.** The FTO glass was first etched using a laser scribe machine. It was then cleaned ultrasonically with detergent, pure water and ethyl alcohol (20 min each). After drying by dry-air blowing, it was treated by ultraviolet ozone (UVO) for 15 min before use. The SnO<sub>2</sub> layer was deposited onto a clean FTO substrate of different sizes by a chemical bath deposition method<sup>24</sup>. Then a 2 M FA<sub>0.88</sub>Cs<sub>0.12</sub>PbI<sub>3</sub>–NMP/DMF perovskite precursor solution with further addition of different additives was simply spin-coated onto SnO<sub>2</sub>/FTO substrates in a nitrogen-filled glovebox (temperature, ~15 °C; relative humidity, <5%) at 5,000 r.p.m. for 60 s. The films were then annealed at 70 °C for 1 min and taken out for further annealing at 150 °C for 10 min in an ambient environment with a relative humidity of ~20–30%. All the achieved perovskite films were treated with 15 mM DABr/IPA solution at 4,000 r.p.m. for 20 s, and then annealed at 100 °C for 5 min. The spiro-OMeTAD solution was spin-coated on the perovskite films at 4,000 rpm for 20 s. Finally, an 80-nm-thick layer of gold was deposited using thermal evaporation to complete the whole device.

**Perovskite solar mini-module fabrication: 5 cm × 5 cm.** The designated P1 pattern of FTO glass was customized by Yingkou OPV Tech New Energy as depicted in Supplementary Fig. 19. It was then cleaned and deposited with an SnO<sub>2</sub> layer as described above. The perovskite films were spin-coated onto the 5 cm × 5 cm substrates and annealed according to the above procedures. It should be noted that it is better to use a gas-assisted method to remove large amounts of volatile DMF gas immediately; otherwise, this will react with the dry film and affect the nucleation process. After the treatment with DABr and spin-coating of spiro-OMeTAD films, the samples were etched by a picosecond laser (Picosecond Laser Processing System, LPS-R002A, Spectronix Corporation). A laser wavelength of 532 nm and a pulse duration of 12 ± 3 ps is used to form a P2 pattern (power, 3.0 W; average fluence, ~0.23 J cm<sup>-2</sup> per pulse) and subsequently to form a P3 pattern (power, 3.8 W; average fluence, ~0.29 J cm<sup>-2</sup> per pulse) according to Supplementary Fig. 19 after evaporation of the gold electrodes.

**Perovskite solar sub-module fabrication: 15 cm × 15 cm.** The designated P1 pattern of FTO glass is depicted in Supplementary Fig. 24. It was cleaned and deposited with an SnO<sub>2</sub> layer as described above. The 1.25 M solution of the perovskite precursor inks were blade coated onto the 15 cm × 15 cm substrates in a simple glovebox in which the local atmosphere was approximately controlled (temperature, 15 ± 5 °C; relative humidity, 15 ± 5%); the films were removed and annealed, first at 70 °C for 1 min and then at 150 °C for 10 min in an ambient environment with a relative humidity of ~20–30%. The perovskite precursor ink was manually supplied to the coater head during the coating process. The distance between the blade-coater head and the substrate was 0.35 mm (*z* = 0.35 mm). The motor rotation frequency for the blade-coating process was set as 500 Hz, corresponding to a coating speed of ~3 mm s<sup>-1</sup>. The angle between the air knife and substrate was about 60°. The nitrogen pressure was set at ~0.3 MPa. A 5 mM DABr/IPA solution was blade coated onto the perovskite substrates, followed by thermal annealing at 100 °C for 5 min. The spiro-OMeTAD solution was also blade coated onto the substrates. The samples were etched with a picosecond laser to form a P2 pattern and etched again to form a P3 pattern according to Supplementary Fig. 24 after evaporation of the gold electrode.

**Photovoltaic performance characterization.** The  $I$ – $V$  characteristics of the perovskite solar cells were measured using a Keithley 2420 source meter in a dry room (temperature,  $15 \pm 5$  °C; relative humidity,  $25 \pm 5$  %). The light source was a solar simulator (Newport Oriol Sol 1A, xenon lamp, USHIO, UXL-150SO) to match AM 1.5 G. The intensity of the light was  $100 \text{ mW cm}^{-2}$  calibrated by using a KG3 reference silicon cell (Enlitech). The EQE spectra were measured by using an Oriol IQE 200. All the devices were tested using a black metal mask with an aperture area of  $0.16 \text{ cm}^2$  for the small devices,  $22.4 \text{ cm}^2$  for the  $5 \text{ cm} \times 5 \text{ cm}$  mini-modules and  $205 \text{ cm}^2$  for the  $15 \text{ cm} \times 15 \text{ cm}$  sub-modules. The  $I$ – $V$  scan range was from  $-0.1$  to  $1.2 \text{ V}$  for the small-size solar cells, from  $-0.1$  to  $8.5 \text{ V}$  for the mini-modules and from  $-0.5$  to  $25 \text{ V}$  for the sub-modules. The corresponding  $I$ – $V$  (or  $J$ – $V$ ) curves were measured at scan rates of  $\sim 0.2 \text{ V s}^{-1}$  for the small-area solar cells,  $\sim 0.8 \text{ V s}^{-1}$  for the  $5 \text{ cm} \times 5 \text{ cm}$  mini-modules and  $\sim 2.0 \text{ V s}^{-1}$  for the  $15 \text{ cm} \times 15 \text{ cm}$  sub-modules without preconditioning.

**Light stability testing.** The perovskite solar cells under MPP and mini-modules under MPPT were tested in our home-designed environmental enclosure box under a flow of dry nitrogen to keep the relative humidity below 5% (Supplementary Fig. 26). The devices were illuminated by a solar simulator (PEC-L01, Peccel) and the power output was measured continuously using a source meter (Keithley 2401) controlled by a program written in Labview. The algorithm used for MPPT is based on perturbation–observation. It starts by applying the maximum voltage derived from the first  $I$ – $V$  curve (Fig. 5d), then the applied voltage is perturbed every minute with a small voltage variation to search for the MPP, and the corresponding maximum voltage, maximum current and maximum power are recorded.

**Characterization.** The surface morphologies of the perovskite films and the cross-sectional structure of the PSCs were investigated by SEM (FEI Quanta 250 FEG FEI Quanta 250 FEG). The X-ray photoelectron spectroscopy and ultraviolet photoemission spectroscopy measurements were conducted with a photoelectron spectrometer (AXIS Ultra HAS, Kratos) equipped with monochromatic Al K $\alpha$  (1,486.6 eV) and non-monochromatic He I (21.22 eV) sources, respectively. X-ray diffraction (Bruker D8 Discover), ultraviolet–visible spectrometry (V-670, JASCO), time-resolved confocal photoluminescence microscopy (Micro Time 200, PicoQuant GmbH) and mass spectrometry (HAL 3F-510, Hidden Analytical) were used for the characterization of the perovskite films. The atomic force microscopy topography images in Supplementary Fig. 11b were acquired with an atomic force microscope (Park NX10) in non-contact mode using a silicon cantilever with a nominal spring constant of  $42 \text{ N m}^{-1}$  (PPP-NCHR). The atomic force microscopy topography images in Supplementary Figs. 20e, 21d and 22d were acquired with an atomic force microscope (Asylum Research MFP-3D) in tapping mode using a silicon cantilever with a nominal spring constant of  $48 \text{ N m}^{-1}$  (Budget Sensors Tap190Al-G).

**Computational methods.** All calculations were carried on the basis of the projector-augmented wave method as implemented in the Vienna Ab initio Simulation Package (VASP) code<sup>40–42</sup>. The Perdew–Burke–Ernzerhof functional within the generalized gradient approximation was employed to describe the exchange–correlation interaction<sup>43</sup>. Van der Waals correction proposed by the Grimme potential (D2) was considered<sup>44</sup>. The plane-wave basis cut-off energy was set to be  $400 \text{ eV}$ . The Monkhorst–Pack  $k$ -point mesh was sampled with a separation of about  $0.015 \text{ \AA}^{-1}$  in the Brillouin zone. All structures were relaxed until the residual force on each atom was less than  $0.01 \text{ eV \AA}^{-1}$ . The self-consistent convergence accuracy was set at  $10^{-5} \text{ eV}$  per atom in the structural calculation. The numerical calculations in this paper have been done on the HPC system of Xidian University. All the crystallographic information files of the structure models, including  $\alpha$ -FAPbI<sub>3</sub> (CCDC#1532918),  $\delta$ -FAPbI<sub>3</sub> (CCDC#968115), PbI<sub>2</sub> (CCDC#77324),  $\alpha$ -CsPbI<sub>3</sub> (CCDC#161481),  $\delta$ -CsPbI<sub>3</sub> (CCDC#161480), PbI<sub>2</sub>–DMF (CCDC#1505389) and PbI<sub>2</sub>–NMP (CCDC#1915704), were obtained from the Cambridge Crystallographic Data Centre (CCDC) public database at [http://www.ccdc.cam.ac.uk/data\\_request/cif](http://www.ccdc.cam.ac.uk/data_request/cif) and refs.<sup>45–48</sup>.

**Reporting summary.** Further information on the research design is available in the Nature Research Reporting Summary linked to this article.

## Data availability

All data generated or analysed during this study are included in the published article and its Supplementary Information. Source Data and Supplementary Data are provided with this paper. Source data are provided with this paper.

Received: 26 October 2021; Accepted: 27 April 2022;  
Published online: 2 June 2022

## References

- Yoo, J. J. et al. Efficient perovskite solar cells via improved carrier management. *Nature* **590**, 587–593 (2021).
- Jeong, J. et al. Pseudo-halide anion engineering for  $\alpha$ -FAPbI<sub>3</sub> perovskite solar cells. *Nature* **592**, 381–385 (2021).
- Min, H. et al. Perovskite solar cells with atomically coherent interlayers on SnO<sub>2</sub> electrodes. *Nature* **598**, 444–450 (2021).
- Park, N.-G. & Zhu, K. Scalable fabrication and coating methods for perovskite solar cells and solar modules. *Nat. Rev. Mater.* **5**, 333–350 (2020).
- Li, Z. et al. Scalable fabrication of perovskite solar cells. *Nat. Rev. Mater.* **3**, 18017 (2018).
- Lee, J. W., Lee, D. K., Jeong, D. N. & Park, N. G. Control of crystal growth toward scalable fabrication of perovskite solar cells. *Adv. Funct. Mater.* **29**, 1807047 (2018).
- Lee, S. W., Bae, S., Kim, D. & Lee, H. S. Historical analysis of high-efficiency, large-area solar cells: toward upscaling of perovskite solar cells. *Adv. Mater.* **32**, e2002202 (2020).
- Qiu, L., He, S., Ono, L. K., Liu, S. & Qi, Y. B. Scalable fabrication of metal halide perovskite solar cells and modules. *ACS Energy Lett.* **4**, 2147–2167 (2019).
- Howard, I. A. et al. Coated and printed perovskites for photovoltaic applications. *Adv. Mater.* **31**, e1806702 (2019).
- Deng, Y. et al. Defect compensation in formamidinium–caesium perovskites for highly efficient solar mini-modules with improved photostability. *Nat. Energy* **6**, 633–641 (2021).
- Tang, S. et al. Composition engineering in doctor-blading of perovskite solar cells. *Adv. Energy Mater.* **7**, 1700302 (2017).
- Tong, G. et al. Removal of residual compositions by powder engineering for high efficiency formamidinium-based perovskite solar cells with operation lifetime over 2000 h. *Nano Energy* **87**, 106152 (2021).
- Jung, E. H. et al. Efficient, stable and scalable perovskite solar cells using poly(3-hexylthiophene). *Nature* **567**, 511–515 (2019).
- Qiu, L. et al. Scalable fabrication of stable high efficiency perovskite solar cells and modules utilizing room temperature sputtered SnO<sub>2</sub> electron transport layer. *Adv. Funct. Mater.* **29**, 1806779 (2018).
- Bu, T. et al. Universal passivation strategy to slot-die printed SnO<sub>2</sub> for hysteresis-free efficient flexible perovskite solar module. *Nat. Commun.* **9**, 4609 (2018).
- Liu, Z. et al. A holistic approach to interface stabilization for efficient perovskite solar modules with over 2,000-hour operational stability. *Nat. Energy* **5**, 596–604 (2020).
- Dagar, J. et al. Compositional and interfacial engineering yield high-performance and stable p-i-n perovskite solar cells and mini-modules. *ACS Appl. Mater. Interfaces* **13**, 13022–13033 (2021).
- Hanul, Min et al. Efficient, stable solar cells by using inherent bandgap of  $\alpha$ -phase formamidinium lead iodide. *Science* **366**, 749–753 (2019).
- Min, H., Jeong, J. et al. Stable perovskite solar cells with efficiency exceeding 24.8% and 0.3-V voltage loss. *Science* **369**, 1615–1620 (2020).
- Turren-Cruz, S.-H., Hagfeldt, A. & Saliba, M. Methylammonium-free, high-performance, and stable perovskite solar cells on a planar architecture. *Science* **362**, 449–453 (2018).
- Qiu, L. et al. Hybrid chemical vapor deposition enables scalable and stable Cs–FA mixed cation perovskite solar modules with a designated area of  $91.8 \text{ cm}^2$  approaching 10% efficiency. *J. Mater. Chem. A* **7**, 6920–6929 (2019).
- Zhang, J. et al. Two-step sequential blade-coating of high quality perovskite layers for efficient solar cells and modules. *J. Mater. Chem. A* **8**, 8447–8454 (2020).
- Yang, Z. et al. Slot-die coating large-area formamidinium–cesium perovskite film for efficient and stable parallel solar module. *Sci. Adv.* **7**, eabg3749 (2021).
- Bu, T. et al. Lead halide–templated crystallization of methylamine-free perovskite for efficient photovoltaic modules. *Science* **372**, 1327–1332 (2021).
- Zeng, L. et al. Controlling the crystallization dynamics of photovoltaic perovskite layers on larger-area coatings. *Energy Environ. Sci.* **13**, 4666–4690 (2020).
- Saki, Z., Byranvand, M. M., Taghavinia, N., Kedia, M. & Saliba, M. Solution-processed perovskite thin-films: the journey from lab- to large-scale solar cells. *Energy Environ. Sci.* **14**, 5690–5722 (2021).
- Rong, Y. et al. Toward industrial-scale production of perovskite solar cells: screen printing, slot-die coating, and emerging techniques. *J. Phys. Chem. Lett.* **9**, 2707–2713 (2018).
- Chen, S. et al. Stabilizing perovskite–substrate interfaces for high-performance perovskite modules. *Science* **373**, 902–907 (2021).
- Yoo, J. W. et al. Efficient perovskite solar mini-modules fabricated via bar-coating using 2-methoxyethanol-based formamidinium lead tri-iodide precursor solution. *Joule* **5**, 2420–2436 (2021).
- Petrov, A. A. et al. Formamidinium haloplumbate intermediates: the missing link in a chain of hybrid perovskites crystallization. *Chem. Mater.* **32**, 7739–7745 (2020).
- Yi, C. et al. Entropic stabilization of mixed A-cation ABX<sub>3</sub> metal halide perovskites for high performance perovskite solar cells. *Energy Environ. Sci.* **9**, 656–662 (2016).
- Syzgantseva, O. A., Saliba, M., Gratzel, M. & Rothlisberger, U. Stabilization of the perovskite phase of formamidinium lead triiodide by methylammonium, Cs, and/or Rb doping. *J. Phys. Chem. Lett.* **8**, 1191–1196 (2017).

33. Saidaminov, M. I. et al. Suppression of atomic vacancies via incorporation of isovalent small ions to increase the stability of halide perovskite solar cells in ambient air. *Nat. Energy* **3**, 648–654 (2018).
34. Kim, M. et al. Methylammonium chloride induces intermediate phase stabilization for efficient perovskite solar cells. *Joule* **3**, 2179–2192 (2019).
35. Zhu, T., Zheng, D., Rager, M.-N. & Pauporté, T. The stabilization of formamidinium lead tri-iodide perovskite through a methylammonium-based additive for high-efficiency solar cells. *Sol. RRL* **4**, 2000348 (2020).
36. Ye, F. et al. Roles of MACl in sequentially deposited bromine-free perovskite absorbers for efficient solar cells. *Adv. Mater.* **33**, e2007126 (2021).
37. Wu, C. et al. Crystallization of  $\text{HC}(\text{NH}_2)_2\text{PbI}_3$  black polymorph by solvent intercalation for low temperature solution processing of perovskite solar cells. *J. Phys. Chem. C* **120**, 26710–26719 (2016).
38. Kim, Y. C. et al. Beneficial effects of  $\text{PbI}_2$  incorporated in organo-lead halide perovskite solar cells. *Adv. Energy Mater.* **6**, 1502104 (2016).
39. Ng, A. et al. A cryogenic process for antisolvent-free high-performance perovskite solar cells. *Adv. Mater.* **30**, e1804402 (2018).
40. Kohn, W. & Sham, L. J. Self-consistent equations including exchange and correlation effects. *Phys. Rev. A* **140**, 1133–1138 (1965).
41. Kresse, G. & Joubert, D. P. From ultrasoft pseudopotentials to the projector augmented-wave method. *Phys. Rev. B* **59**, 1758–1775 (1999).
42. Blochl, P. E. Projector augmented-wave method. *Phys. Rev. B* **50**, 17953–17979 (1994).
43. Perdew, JohnP., Burke, Kieron & Ernzerhof, M. Generalized gradient approximation made simple. *Phys. Rev. Lett.* **27**, 1787–1799 (2006).
44. Grimme, S. Semiempirical GGA-type density functional constructed with a long-range dispersion correction. *J. Comput. Chem.* **27**, 1787–1799 (2006).
45. Huang, Y. et al. The intrinsic properties of  $\text{FA}_{(1-x)}\text{MA}_x\text{PbI}_3$  perovskite single crystals. *J. Mater. Chem. A* **5**, 8537–8544 (2017).
46. Stoumpos, C. C., Malliakas, C. D. & Kanatzidis, M. G. Semiconducting tin and lead iodide perovskites with organic cations: phase transitions, high mobilities, and near-infrared photoluminescent properties. *Inorg. Chem.* **52**, 9019–9038 (2013).
47. Marronnier, A. et al. Anharmonicity and disorder in the black phases of cesium lead iodide used for stable inorganic perovskite solar cells. *ACS Nano* **12**, 3477–3486 (2018).
48. Trots, D. M. & Myagkota, S. V. High-temperature structural evolution of caesium and rubidium triiodoplumbates. *J. Phys. Chem. Solids* **69**, 2520–2526 (2008).
49. Hu, Y. et al. Standardizing perovskite solar modules beyond cells. *Joule* **3**, 2076–2085 (2019).

## Acknowledgements

This work was supported by funding from the Energy Materials and Surface Sciences Unit of the Okinawa Institute of Science and Technology Graduate University, the OIST R&D Cluster Research Program, the OIST Proof of Concept (POC) Program and JST A-STEP grant number JPMJTM20HS, Japan. We thank the OIST Micro/Nanofabrication Section and Imaging Section for the support.

## Author contributions

Y.B.Q. supervised the project. Y.B.Q. and T.B. conceived the ideas. T.B. designed the experiments and conducted the corresponding device and module fabrication and characterization. L.K.O. contributed to part of the characterization and analyses. J.L. helped with the X-ray diffraction and time-resolved photoluminescence mapping characterization. J.S. conducted the density functional theory calculations. G.T. helped with the stability test. Y.B.Q. contributed to part of the atomic force microscopy measurements. J.Z. contributed to part of the perovskite solar cell measurements. Y.L., S.K., W.Z., J.C., F.H. and Y.-B.C. provided valuable suggestions for the manuscript. Y.B.Q. and T.B. participated in all of the data analyses. Y.B.Q. and T.B. wrote the paper, and all authors revised the paper.

## Competing interests

The authors declare no competing interests.

## Additional information

**Supplementary information** The online version contains supplementary material available at <https://doi.org/10.1038/s41560-022-01039-0>.

**Correspondence and requests for materials** should be addressed to Yabing Qi.

**Peer review information** *Nature Energy* thanks Francesco Di Giacomo, Jin Young Kim and the other, anonymous, reviewer(s) for their contribution to the peer review of this work.

**Reprints and permissions information** is available at [www.nature.com/reprints](http://www.nature.com/reprints).

**Publisher's note** Springer Nature remains neutral with regard to jurisdictional claims in published maps and institutional affiliations.

© The Author(s), under exclusive licence to Springer Nature Limited 2022

## Solar Cells Reporting Summary

Nature Research wishes to improve the reproducibility of the work that we publish. This form is intended for publication with all accepted papers reporting the characterization of photovoltaic devices and provides structure for consistency and transparency in reporting. Some list items might not apply to an individual manuscript, but all fields must be completed for clarity.

For further information on Nature Research policies, including our [data availability policy](#), see [Authors & Referees](#).

## ▶ Experimental design

## Please check: are the following details reported in the manuscript?

## 1. Dimensions

Area of the tested solar cells  Yes  No  
The active area of small-size perovskite solar cells is 0.16 cm<sup>2</sup>. The aperture area of perovskite mini-modules on 25 cm<sup>2</sup> substrate is 22.4 cm<sup>2</sup> and sub-modules on 225 cm<sup>2</sup> substrate is 205 cm<sup>2</sup>. The information can be found in the Photovoltaic characterization part in Method.

Method used to determine the device area  Yes  No  
The small-size perovskite solar cells were measured using a metal mask with the aperture area of 0.16 cm<sup>2</sup>. The large-size perovskite mini-modules and sub-modules were tested using metal masks with the aperture area of 22.4 cm<sup>2</sup> and 205 cm<sup>2</sup>, respectively. The information can be found in the Photovoltaic characterization part in Method.

## 2. Current-voltage characterization

Current density-voltage (J-V) plots in both forward and backward direction  Yes  No  
The J-V curves were scanned in the reverse direction unless specified otherwise. The J-V curves for the hysteresis study are obtained from scans in both forward and backward directions. The information can be found in the Photovoltaic characterization part in Method and the plots are showed in Supplementary Information.

Voltage scan conditions  Yes  No  
*For instance: scan direction, speed, dwell times*  
The corresponding I-V (or J-V) curves were measured at scan rates of ~0.2 V s<sup>-1</sup> for the small-area solar cells, ~0.8 V s<sup>-1</sup> for the 5 cm × 5 cm mini-modules and ~2.0 V s<sup>-1</sup> for the 15 cm × 15 cm sub-modules respectively without preconditioning. The information can be found in the Photovoltaic characterization part in Method.

Test environment  Yes  No  
*For instance: characterization temperature, in air or in glove box*  
The J-V curves were measured in the dry room (15 ± 5 °C, 25 ± 5 % relative humidity). The information can be found in the Photovoltaic characterization part in Method.

Protocol for preconditioning of the device before its characterization  Yes  No  
Measurement of initial PCE without preconditioning was aimed in our studies.

Stability of the J-V characteristic  Yes  No  
*Verified with time evolution of the maximum power point or with the photocurrent at maximum power point; see ref. 7 for details.*  
Stabilized photocurrent output by holding the voltage at the maximum power point for perovskite solar cells and modules (Supplementary Figure 17, 22 and 25).

## 3. Hysteresis or any other unusual behaviour

Description of the unusual behaviour observed during the characterization  Yes  No  
Hysteresis characterization were provided in Fig 4. The optimized device shows no hysteresis because of the potassium passivation.

Related experimental data  Yes  No  
Forward and reverse scans for characterizing hysteresis were provided in Figure 4 and Supplementary Figure 17.

## 4. Efficiency

External quantum efficiency (EQE) or incident photons to current efficiency (IPCE)  Yes  No  
The EQE of small size device is shown in Figure 4c.

A comparison between the integrated response under the standard reference spectrum and the response measure under the simulator  Yes  No  
The integrated current densities from the EQE curve are matched well with the measured J<sub>sc</sub> value. This is stated in the device performance discussion part.

For tandem solar cells, the bias illumination and bias voltage used for each subcell	<input type="checkbox"/> Yes <input checked="" type="checkbox"/> No	No tandem solar cells were fabricated in this work.
<b>5. Calibration</b>		
Light source and reference cell or sensor used for the characterization	<input checked="" type="checkbox"/> Yes <input type="checkbox"/> No	Solar simulator (Newport Oriel Sol 1A, xenon lamp, USHIO, UXL-150SO) matching AM 1.5 G was employed in this work. The intensity of the light is 100 mW cm <sup>-2</sup> calibrated by using a KG3 reference silicon cell (Enlitech). The information can be found in the Photovoltaic characterization part in Method.
Confirmation that the reference cell was calibrated and certified	<input checked="" type="checkbox"/> Yes <input type="checkbox"/> No	The KG3 reference silicon cell purchased from Enlitech are calibrated ( <a href="https://www.newport.com/p/91150-KG3">https://www.newport.com/p/91150-KG3</a> ). The information can be found in the photovoltaic characterization part in Method.
Calculation of spectral mismatch between the reference cell and the devices under test	<input type="checkbox"/> Yes <input checked="" type="checkbox"/> No	No spectral mismatch calculation was performed.
<b>6. Mask/aperture</b>		
Size of the mask/aperture used during testing	<input checked="" type="checkbox"/> Yes <input type="checkbox"/> No	All the devices were tested using a black metal mask with an aperture area of 0.16 cm <sup>2</sup> for the small devices and 22.4 cm <sup>2</sup> for the 5 cm × 5 cm mini-modules and 205 cm <sup>2</sup> for the 15 cm × 15 cm sub-modules, respectively. The information can be found in the Photovoltaic characterization part in Method.
Variation of the measured short-circuit current density with the mask/aperture area	<input type="checkbox"/> Yes <input checked="" type="checkbox"/> No	<i>Explain why this information is not reported/not relevant.</i>
<b>7. Performance certification</b>		
Identity of the independent certification laboratory that confirmed the photovoltaic performance	<input type="checkbox"/> Yes <input checked="" type="checkbox"/> No	<i>Explain why this information is not reported/not relevant.</i>
A copy of any certificate(s) <i>Provide in Supplementary Information</i>	<input type="checkbox"/> Yes <input checked="" type="checkbox"/> No	<i>Explain why this information is not reported/not relevant.</i>
<b>8. Statistics</b>		
Number of solar cells tested	<input checked="" type="checkbox"/> Yes <input type="checkbox"/> No	The information can be found in the Supplementary Figure 16 in Supplementary Information.
Statistical analysis of the device performance	<input checked="" type="checkbox"/> Yes <input type="checkbox"/> No	Statistical analysis of the photovoltaic parameters for 15 small size devices (Supplementary Figure 16) and 20 sub-module devices (Supplementary Figure 25) are provided and in Supplementary Information.
<b>9. Long-term stability analysis</b>		
Type of analysis, bias conditions and environmental conditions <i>For instance: illumination type, temperature, atmosphere humidity, encapsulation method, preconditioning temperature</i>	<input checked="" type="checkbox"/> Yes <input type="checkbox"/> No	See the Light stability testing in Method part.